Frequency Space Environment Map Rendering

Ravi Ramamoorthi Pat Hanrahan

Stanford University *

Figure 1: *These images, showing many different lighting conditions and BRDFs, were each rendered at approximately 30 frames per second using our Spherical Harmonic Reflection Map (SHRM) representation. From left to right, a simplified microfacet BRDF, krylon blue (using McCool et al.'s reconstruction from measurements at Cornell), orange and velvet (CURET database), and an anisotropic BRDF (based on the Kajiya-Kay model). The environment maps are the Grace Cathedral, St. Peter's Basilica, the Uffizi gallery, and a Eucalyptus grove, courtesy Paul Debevec. The armadillo model is from Venkat Krishnamurthy.*

Abstract

We present a new method for real-time rendering of objects with complex isotropic BRDFs under distant natural illumination, as specified by an environment map. Our approach is based on spherical frequency space analysis and includes three main contributions. Firstly, we are able to theoretically analyze required sampling rates and resolutions, which have traditionally been determined in an ad-hoc manner. We also introduce a new compact representation, which we call a *spherical harmonic reflection map (SHRM)*, for efficient representation and rendering. Finally, we show how to rapidly prefilter the environment map to compute the *SHRM*—our frequency domain prefiltering algorithm is generally orders of magnitude faster than previous angular (spatial) domain approaches.

CR Categories: I.3.7 [*Computer Graphics*]: Three-Dimensional Graphics and Realism—Environment Maps

Keywords: Environment Maps, Image-Based Rendering, Signal-Processing, Complexity Analysis, Spherical Harmonics.

1 Introduction

Our goals are real-time rendering with complex natural illumination and realistic, possibly measured, BRDFs. The closest previous work is that of Cabral et al. [1999], who extended standard environment maps by interactively warping and combining a sparse 2D set of prerendered images. These precomputed images were obtained by *prefiltering* the environment map, i.e. integrating the product of the BRDF and lighting over the visible (upper) hemisphere for each image pixel, with each pixel corresponding to a particular surface normal direction. Subsequently, [Kautz and McCool 2000; Kautz et al. 2000] proposed alternative implementations and improved prefiltering methods.

This paper introduces a new frequency space paradigm for prefiltering and rendering environment mapped images with general isotropic BRDFs. Our approach is based on recent theoretical results by Basri and Jacobs [2001] and Ramamoorthi and Hanrahan [2001b; 2001c], wherein they formalize the notion of reflection as a spherical convolution of the illumination and BRDF. We show that frequency space analysis allows for setting sampling rates accurately, and enables compact representations. Further, just as image convolutions are often computed in the Fourier rather than the spatial domain, prefiltering is more efficient in frequency rather than angular space. Our main contributions are:

Theoretical analysis of sampling rates and resolutions: Most previous work has determined reflection map resolutions, or the number of reflection maps required, in an ad-hoc manner. By using a signal-processing framework, we are able to perform error analysis, that allows us to set sampling rates and resolutions accurately.

Efficient representation and rendering with Spherical Harmonic Reflection Maps: We introduce *spherical harmonic reflection maps (SHRMs)* as a compact representation. Instead of a single color, each pixel stores coefficients of a spherical harmonic expansion encoding view-dependence of the reflection map. A key insight that emerges from the theoretical analysis is that for almost all BRDFs, a very low order spherical harmonic expansion suffices. Thus, SHRMs can be evaluated in real-time for rendering. Further, they are significantly more compact and accurate than previous methods [Cabral et al. 1999; Kautz and McCool 2000] that use an explicit 1D or 2D set of images.

Fast prefiltering: One of the drawbacks of current environment mapping techniques is the significant computational time required for prefiltering, which can run into hours, and preclude the use of these approaches in applications involving lighting and material design, or dynamic lighting. We introduce new prefiltering methods based on spherical harmonic transforms, and show both empirically, and analytically by computational complexity analysis, that our algorithms are orders of magnitude faster than previous work.

We present a complete theoretical analysis and practical algorithm pipeline, incorporating all three contributions. It is also possible to separately (incrementally) incorporate any one (or two) of the improvements into previous methods.

2 Related Work

Angular space environment map rendering has a long history in graphics, including early work by Blinn and Newell [1976], Miller and Hoffman [1984], and Greene [1986]. Hakura et al. [2001] propose location and geometry-dependent environment maps for local reflections. Our goals are different in that we want to capture the effects of complex BRDFs and use any object geometry, but it should be possible in future to combine the methods for local reflections

* (ravir,hanrahan)@graphics.stanford.edu

Copyright © 2002 by the Association for Computing Machinery, Inc.
Permission to make digital or hard copies of part or all of this work for personal or classroom use is granted without fee provided that copies are not made or distributed for commercial advantage and that copies bear this notice and the full citation on the first page. Copyrights for components of this work owned by others than ACM must be honored. Abstracting with credit is permitted. To copy otherwise, to republish, to post on servers, or to redistribute to lists, requires prior specific permission and/or a fee. Request permissions from Permissions Dept, ACM Inc., fax +1-212-869-0481 or e-mail permissions@acm.org.
© 2002 ACM 1-58113-521-1/02/0007 $5.00

$\vec{L}, \vec{N}, \vec{V}, \vec{R}$	Global incident, normal, viewing, reflected directions
$\vec{\omega}_i, \vec{\omega}_o$	Local incident, outgoing (viewing) directions
(α, β)	Elevation, azimuthal angles for $\vec{N}$ (or $\vec{R}$)
$R_{\alpha,\beta}$	Rotation operator for surface orientation (α, β)
(θ_i, ϕ_i)	Local incident elevation and azimuthal angles ($\vec{\omega}_i$)
(θ_o, ϕ_o)	Local outgoing elevation and azimuthal angles ($\vec{\omega}_o$)
$(\tilde{\theta}_o, \tilde{\phi}_o)$	Global outgoing angles ($\vec{V}$)
$d\omega_i, \Omega$	(Differential) hemisphere of integration
L, B	Incident, Reflected radiance
$\rho, \hat{\rho}$	BRDF, BRDF multiplied by cosine of incident angle
$L_{lm}, \hat{\rho}_l, \hat{\rho}_{lpq}$	Coefficients in spherical harmonic expansion of L,$\hat{\rho}$
B_{lm}, B_{lmpq}	Coefficients in basis-function expansion of B
$B_{pq}(\alpha, \beta)$	Coefficients in SHRM
$D^l_{mn}(\alpha)$	Matrix for rotating spherical harmonics
$Y_{lm}(\theta, \phi)$	Spherical Harmonic basis function
$Y^*_{lm}(\theta, \phi)$	Complex Conjugate of Spherical Harmonic
$f_{lm}(\theta)$	Normalized θ dependence of Y_{lm}
s, σ	Phong exponent, surface roughness (microfacet)
Λ_l	$\sqrt{4\pi/(2l+1)}$
I	$\sqrt{-1}$
F	Maximum order l of coefficients $\hat{\rho}_{lpq}$,B_{lmpq}
P	Maximum order p in spherical harmonic expansion
S	Angular resolution $(S > F)$
T	Number of images in angular space $(T > P)$
W	Angular width of BRDF
ϵ	Error (unaccounted energy in approximation)
C_a, C_f	Angular, frequency domain computational costs

Table 1: *Notation used in the paper.*

and complex BRDFs. Most recently, we [Ramamoorthi and Hanrahan 2001a] applied spherical harmonic analysis to irradiance environment maps for Lambertian objects. This paper generalizes that approach to general isotropic materials.

As noted by Cabral et al. [1999], environment mapping can be viewed as reflection-space image-based rendering, and is therefore related to a number of IBR methods like surface light fields [Nishino et al. 1999; Wood et al. 2000]. A surface light field stores the outgoing radiance distribution for each point on a geometric model. We store the reflected radiance distribution for each normal direction, allowing our representation to be mapped on to any object geometry. Our representation is essentially equivalent to the surface light field of a sphere, or an *orientation light field*.

Our work also relates to recent research on hardware rendering with factored BRDFs [Kautz and McCool 1999; McCool et al. 2001]. However, these methods require the BRDF to at least approximately satisfy a particular factored form. These previous methods also do not support complex illumination.

We use spherical harmonics—the analogue on the sphere to the Fourier basis, i.e. sines and cosines, on the line or circle. Spherical harmonics were first used in graphics in early work by Cabral et al. [1987], and later by Sillion et al. [1991] and Westin et al. [1992].

3 Preliminaries

In this section, we first discuss the reflection equation and introduce the basic framework for our method. We then describe our BRDF parameterization, and discuss previous 4D function representations. Table 1 summarizes notation used in the paper, and appendix A gives the main spherical convolution formulae [Ramamoorthi and Hanrahan 2001b; Ramamoorthi and Hanrahan 2001c].

Assumptions: We make a number of simplifying assumptions common in real-time rendering in general, and environment mapping in particular. Specifically, we assume distant illumination and isotropic BRDFs, and restrict ourselves to direct lighting, ignoring interreflection and self-shadowing. We will also not explicitly considered textured objects, but it is easy to use texture-mapping to modulate the net reflectance, simply by multiplying the texture and the reflected light field computed by our methods.

Reflection Equation: Given our assumptions, the reflected light field can be written simply as a function of the surface orientation $\vec{N}$ and outgoing direction $\vec{\omega}_o$ with respect to the local surface:

$$B(\vec{N}; \vec{\omega}_o) = \int_\Omega L(\vec{N}; \vec{\omega}_i)\rho(\vec{\omega}_i, \vec{\omega}_o)(\vec{\omega}_i \cdot \vec{z})\, d\omega_i \qquad (1)$$

Here, L is the incident radiance, ρ is the BRDF, and B is the reflected light field. $\vec{N}$ corresponds to the *global* coordinates of the surface normal. $\vec{\omega}_i$ and $\vec{\omega}_o$ are *local* incident and outgoing directions, with $\vec{\omega}_i \cdot \vec{z}$ being the cosine of the incident angle (in local coordinates, the surface normal is the $\vec{z}$ vector). Under the assumption of distant illumination, L depends only on the global light direction, obtained by applying a rotation to the local incident direction. We now rewrite equation 1 using the spherical angular parameters (α, β) for $\vec{N}$, (θ_i, ϕ_i) for $\vec{\omega}_i$, and (θ_o, ϕ_o) for $\vec{\omega}_o$. Finally, we assume isotropy, and define $\hat{\rho} = \rho \cos\theta_i$.

$$B(\alpha, \beta; \theta_o, \phi_o) = \int_\Omega L\left(R_{\alpha,\beta}\left(\theta_i, \phi_i\right)\right) \hat{\rho}(\theta_i, \theta_o, \mid \phi_o - \phi_i \mid)\, d\omega_i \qquad (2)$$

When the viewer is distant, it is often useful to rewrite the reflected light field in terms of the global viewing direction $\vec{V} = (\tilde{\theta}_o, \tilde{\phi}_o)$.

$$\begin{aligned} (\theta_o, \phi_o) &= R^{-1}_{\alpha,\beta}\left(\tilde{\theta}_o, \tilde{\phi}_o\right) \\ \tilde{B}\left(\alpha, \beta; \tilde{\theta}_o, \tilde{\phi}_o\right) &= B\left(\alpha, \beta; R^{-1}_{\alpha,\beta}\left(\tilde{\theta}_o, \tilde{\phi}_o\right)\right) \qquad (3) \end{aligned}$$

Our general approach (and that of previous work [Cabral et al. 1999; Kautz and McCool 2000]) is to represent the incident lighting L by an environment map. The environment map is *prefiltered* to compute some representation of B (or $\tilde{B}$), followed by interactive *rendering* with this representation.

The rest of this paper covers a number of issues that must be addressed. First, we must find the appropriate (re)parameterization for B and $\hat{\rho}$. Next, we must determine how to represent B in a compact manner suitable for interactive rendering. For this, it is important to analyze the required sampling rates and output resolutions. Finally, we must determine how to efficiently compute our representation of B, i.e. rapidly prefilter the environment map. An overview of our entire algorithm pipeline is shown in figure 3.

3.1 Reparameterization by central BRDF direction

Our goal is to reparameterize the BRDF and reflected light field so that they become relatively simple and compact, and possibly lower-dimensional functions. Reparameterizing also allows us to eliminate the warping step required by Cabral et al. [1999].

Consider first the special case of *radially symmetric or 1D BRDFs*, where the BRDF consists of a single symmetric lobe of fixed shape, whose orientation depends only on a well-defined central direction $\vec{C}$. In other words, the BRDF is given by a 1D function u as $\hat{\rho} = u(\vec{C} \cdot \vec{L})$. Examples are Lambertian $\hat{\rho} = \vec{N} \cdot \vec{L}$ and Phong $\hat{\rho} = (\vec{R} \cdot \vec{L})^s$ models. If we reparameterize by $\vec{C}$, the BRDF becomes a function of only 1 variable (θ_i with $\cos\theta_i = \vec{C} \cdot \vec{L}$) instead of 3. Further, the reflected light field can be represented simply by a 2D reflection map $B(\alpha, \beta)$ parameterized by $\vec{C} = (\alpha, \beta)$. Note that we will often use $\vec{R}$, the reflection of the viewing direction about the surface normal, as a synonym for $\vec{C}$ since that is the most common case; however our analysis applies generally.

For general BRDFs, the radial symmetry property does not hold precisely, so they cannot be reduced exactly to 1D functions, nor can B be written simply as a 2D reflection map. Nevertheless, a reparameterization by the reflection vector still yields compact forms. As can be seen for the $\vec{N} \cdot \vec{H}$ model shown in the lower part of figure 2, most of the variation in the BRDF is still over only a single variable (θ_i) after reparameterization, while there is very little variation over θ_o (or ϕ) for fixed θ_i. Further, most of the variation in B remains over (α, β), with only low-frequency variation over the other two variables (θ_o, ϕ_o).

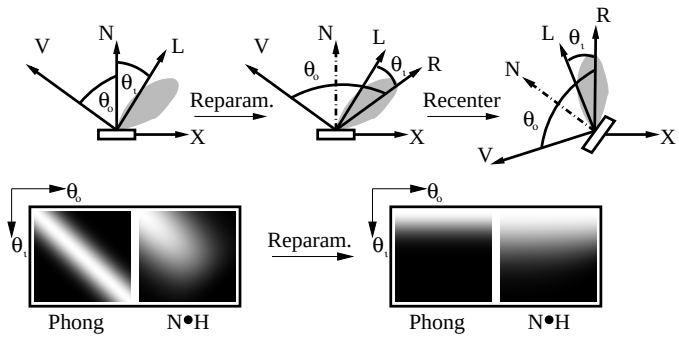

Figure 2: *Reparameterization involves recentering about the reflection vector. BRDFs become more compact, and in special cases (Phong) become 1D functions.*

To reparameterize, we simply recenter the BRDF (and the reflection integral) about the reflection vector, rather than the surface normal, as shown in figure 2. The reflection vector now takes the place of the surface normal, i.e. $\vec{R} = (\alpha, \beta)$, and the dependence on the surface normal becomes indirect (just as the dependence on $\vec{R}$ is indirect in the standard parameterization). The angles θ_i and θ_o are now given with respect to $\vec{R}$ by $\cos\theta_i = \vec{R} \cdot \vec{L}$ and $\cos\theta_o = \vec{R} \cdot \vec{V}$, with $B(\alpha, \beta, \theta_o, \phi_o)$ a function of $\vec{R} = (\alpha, \beta)$ and $\vec{\omega}_o = (\theta_o, \phi_o)$.

Note that, although this paper does not address general 4D anisotropic BRDFs, reparameterization by the tangent vector $\vec{T}$ can be used in special cases to reduce anisotropic BRDFs to 1D or 2D functions, amenable to treatment by our algorithm pipeline. For instance, consider the Kajiya-Kay [1989] model. This BRDF is an anisotropic extension of the Phong model, and depends on $\vec{T} \cdot \vec{L}$ and $\vec{T} \cdot \vec{V}$. We may reparameterize by the tangent vector, just as we did above with the reflection vector. Then, $\cos\theta_i = \vec{T} \cdot \vec{L}$ and $\cos\theta_o = \vec{T} \cdot \vec{V}$, with the BRDF being given by $\hat{\rho} = \cos^s(\theta_i - \theta_o)$. The BRDF is now a simple 2D function, which is only slightly more complex than the reparameterized 1D Phong BRDF.

An important requirement of our reparameterization is that it be suitable for *both* the BRDF $\hat{\rho}$ and the reflected light field B. Thus, Rusinkiewicz's [Rusinkiewicz 1998] reparameterization of BRDFs, based on the half angle vector $\vec{H}$, cannot be used since it is unsuitable for the reflected light field. $\vec{H}$ depends on the incident light direction, while B depends only on the the viewing direction and surface normal (or reflection vector). Our approach is motivated by the "reflective transformation" used by Wood et al. [2000] to reparameterize the outgoing radiance of surface light fields by $\vec{R}$. However, our final representations differ significantly. In their case, the surface light field is parameterized by object geometry and reflection vector $\vec{R}$, while in our case, the "orientation light field" is parameterized by the reflection vector $\vec{R}$ and viewing vector $\vec{V}$.

3.2 4D function representations

Our goal is to compactly represent $B(\alpha, \beta, \theta_o, \phi_o)$ in a manner suitable for interactive rendering, while exploiting its characteristics. As noted previously [Cabral et al. 1999], the variation over (α, β) may be rapid (high-frequency), while that over (θ_o, ϕ_o) is usually slow (low-frequency), reducing to constant (no variation) for radially symmetric 1D BRDFs. There have been a number of representations for 4D functions proposed in the graphics community, primarily for image-based rendering. The main categories are listed below. Table 2 compares tabular, compressed, factored, coefficient-based, as well as our SHRM representation, in terms of simplicity, compactness of the representation, efficiency for rendering, ease of error analysis, and speed for computation (prefiltering).

Explicit tabular representation: We may simply tabulate $B(\alpha, \beta, \theta_o, \phi_o)$ on a 4D grid. Cabral et al. [1999] use a sparse 2D set of standard 2D reflection maps. However, a very large amount of data will be required to accurately tabulate a 4D light field. Cabral et al. [1999] use only 12 reflection maps, trading accuracy for compactness. Kautz and McCool [2000] approximate the BRDF as a 2D function $\hat{\rho} = u(\theta_i, \theta_o)$ having no azimuthal dependence to create a 3D texture $B(\alpha, \beta, \theta_o)$. This lower-dimensional representation is more compact, but loses some generality, and can still require a large amount of data. Interactive rendering with these methods usually simply involves a texture lookup and interpolation.

Method	Simple	Compact	Rendering	Analysis	Speed
Tabular	Yes	No	Yes	No	No
Compressed	No	Yes	Maybe	*	No
Factored	Yes	Yes	Yes	*	No
Coefficients	Yes	Yes	No	Yes	Yes
SHRM	Yes	Yes	Yes	Yes	Yes

Table 2: *Comparison of different 4D representations. The columns stand for simplicity/intuitiveness, compactness, efficiency for rendering, ease of error analysis, and speed of computation (prefiltering). We use $*$ for error analysis of compressed and factored representations because, while error analysis is straightforward, it requires knowledge of a densely sampled 4D light field, and cannot be applied directly.*

Compressed forms: Compression based on vector-quantization or MPEG-like methods can be used to reduce the size of a tabular representation, as done for surface light fields [Wood et al. 2000]. Care must be taken that the compressed form can be rendered interactively. Note that both computation of and error analysis on the compressed form require us to first compute the dense uncompressed 4D light field, which can be a computation and data-intensive operation.

Factored representation: Factorization can be seen as a simple compression technique that yields compact results suitable for interactive rendering using texture mapping. Previous methods that can be seen as factorizations include eigen-textures [Nishino et al. 1999], polynomial texture maps [Malzbender et al. 2001], and BRDF factorizations [Kautz and McCool 1999; McCool et al. 2001]. The 4D light field is written as the sum of a few terms, each being the product of two 2D functions (textures):

$$B(\alpha, \beta, \theta_o, \phi_o) = \sum_a g_a(\alpha, \beta) h_a(\theta_o, \phi_o) \tag{4}$$

Basis function coefficients: Factored representations can be viewed as a basis-function expansion. To see this, we first introduce a representation purely in terms of basis function coefficients:

$$B(\alpha, \beta, \theta_o, \phi_o) = \sum_a \sum_b c_{ab} d_b(\alpha, \beta) h_a(\theta_o, \phi_o)$$

The basis functions are d_b and h_a with coefficients c_{ab}. We need only store c_{ab}, and can evaluate the basis functions procedurally. This is a simple compact form. However, interactive rendering is difficult since there will usually be a large number of coefficients. We may reduce the number of terms by doing the summation over b to get a factored representation identical to equation 4, defining

$$g_a(\alpha, \beta) = \sum_b c_{ab} d_b(\alpha, \beta)$$

4 Spherical Harmonic Reflection Maps

In this section, we introduce the *spherical harmonic reflection map* or SHRM representation, which is a compact factored representation derived from a spherical harmonic basis function expansion. Figure 3 shows an overview of our entire pipeline. S and T stand for angular resolutions while F and P stand for orders of the spherical harmonic expansions, which are determined using the theoretical analysis in section 5. The inputs to the algorithm are tabulated values of the lighting $L(\theta, \phi)$ and 3D isotropic BRDF $\hat{\rho}(\theta_i, \theta_o, \phi)$.

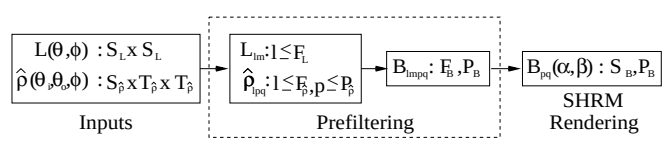

Figure 3: *An overview of our entire pipeline. S and T are angular resolutions, while F and P are orders of the spherical harmonic expansions.*

We then use our fast prefiltering algorithm, described in detail in section 6, to compute the SHRM. This is done by first computing

the spherical harmonic lighting coefficients L_{lm} and BRDF coefficients $\hat{\rho}_{lpq}$. We then use the spherical frequency-space convolution formula [Ramamoorthi and Hanrahan 2001c], which may be viewed as the frequency domain analog of equation 2, to compute reflected light field coefficients B_{lmpq}.

$$B_{lmpq} = \Lambda_l L_{lm} \hat{\rho}_{lpq} \tag{5}$$

Finally, we expand B_{lmpq} to generate the SHRM, as per equation 14 in appendix A.

$$B(\alpha, \beta, \theta_o, \phi_o) = \sum_{p=0}^{P_B} \sum_{q=-p}^{p} B_{pq}(\alpha, \beta) Y_{pq}(\theta_o, \phi_o) \tag{6}$$

In this equation, $B_{pq}(\alpha, \beta)$ is one coefficient in the SHRM, Y_{pq} is the spherical harmonic of order p and index q, and $P_B \geq 0$ is the maximum order of the expansion, with the SHRM containing a total of $(P_B + 1)^2$ terms. Figure 4 illustrates the idea behind SHRMs. Each pixel (α, β) in a reflection (cube)map has a particular distribution of outgoing radiance $B(\alpha, \beta, \theta_o, \phi_o)$. This distribution is encoded by the SHRM as a spherical harmonic expansion in (θ_o, ϕ_o), with coefficients $B_{pq}(\alpha, \beta)$. For the special case of radially symmetric 1D BRDFs, there is no dependence on (θ_o, ϕ_o) after reparameterization, so we need only the DC or constant term $B_{00}(\alpha, \beta)$, and the SHRM reduces to a simple 2D reflection map.

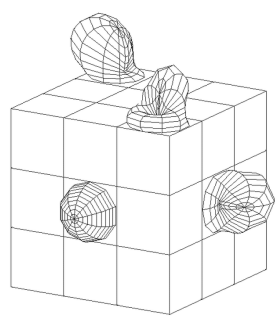

Figure 4: *The idea behind SHRMs. Each pixel (α, β) in the reflection cubemap has some distribution of reflected light. This distribution is encoded as a low-order spherical harmonic expansion in (θ_o, ϕ_o) for every pixel, with coefficients $B_{pq}(\alpha, \beta)$. To avoid clutter, this diagram uses only a 3x3 resolution in the reflection map and shows the outgoing distribution for only four of the pixels.*

So far, we have considered *local* SHRMs, depending on local outgoing angles (θ_o, ϕ_o), which are different for each (α, β). It is often convenient to assume the viewer is distant and compute *global* SHRMs, dependent on a global viewing direction $(\tilde{\theta_o}, \tilde{\phi_o})$.

$$\tilde{B}(\alpha, \beta, \tilde{\theta_o}, \tilde{\phi_o}) = \sum_{p=0}^{P_B} \sum_{q=-p}^{p} \tilde{B}_{pq}(\alpha, \beta) Y_{pq}(\tilde{\theta_o}, \tilde{\phi_o}) \tag{7}$$

The advantage of equation 7 over equation 6 lies in ease of evaluation for rendering, since $Y_{pq}(\tilde{\theta_o}, \tilde{\phi_o})$ can be evaluated once per frame, instead of per pixel. In fact, we will show in section 7.5 that this allows global SHRMs to be rendered using a single dynamic reflection map, with standard reflection mapping hardware.

We still need to know how to determine global SHRM coefficients $\tilde{B}_{pq}(\alpha, \beta)$. The spherical convolution formula in equation 5 applies only to local SHRMs. However, we may rotate coefficients to compute the global SHRM. We make use of equations 3 and 6, with the subscript q changed to s for later convenience.

$$\tilde{B}\left(\alpha, \beta; \tilde{\theta_o}, \tilde{\phi_o}\right) = \sum_{p=0}^{P_B} \sum_{s=-p}^{p} B_{ps}(\alpha, \beta) Y_{ps}\left(R^{-1}_{\alpha,\beta}\left(\tilde{\theta_o}, \tilde{\phi_o}\right)\right)$$

From this expression, we determine the modified (rotated) coefficients of the global SHRM separately for each orientation (α, β), using the spherical harmonic rotational formulae. D^p is a matrix that expresses how rotation about the y axis transforms spherical harmonics into other spherical harmonics of the same order p.

$$\tilde{B}_{pq}(\alpha, \beta) = \sum_{s=-p}^{p} \left(D^p_{sq}(-\alpha) e^{-Iq\beta}\right) B_{ps}(\alpha, \beta) \tag{8}$$

Advantages: SHRMs are a hybrid form, midway between a pure coefficient-based approach, and an explicit tabular representation. We believe this is a good point in the design space, and our representation has the following significant advantages:

- **Compact, Efficient and Accurate:** A key insight from the theoretical analysis is that for essentially all BRDFs, a very low value of P_B (usually ≤ 3) suffices for high accuracy. This is the formal basis for using a low order spherical harmonic expansion in the SHRM, and ensures that our representation is very compact and accurate compared to previous approaches, as well as being efficient to evaluate for real-time rendering.
- **Error analysis and number of coefficients/resolutions:** Unlike for other compression and factorization techniques, the error analysis in section 5 does not first require computation of a dense 4D reflected light field, and allows us to easily determine the correct order P_B of the spherical harmonic expansion and the resolutions of the reflection maps.
- **Rapid computation:** In section 6, we show how the SHRM can be computed using frequency domain prefiltering, orders of magnitude faster than previous approaches.

5 Analysis of sampling rates/resolutions

In this section, we present our framework for analyzing the required sampling rates, i.e. the number of coefficients needed in our spherical harmonic expansions. At the end of the section, we will justify the SHRM representation based on our analysis.

The sampling rates will depend on the frequency content of the lighting and BRDF. Figure 5 shows spheres rendered with progressively blurred illumination (along the y axis) and a progressively more diffuse BRDF (along the x axis). It can be seen that the highest frequencies in the reflected light field are determined approximately by the minimum of the highest frequencies in the lighting and BRDF. This is not surprising, since we may view the BRDF as a low pass filter acting on the lighting signal.

As summarized in figure 3, we assume the input lighting $L(\theta, \phi)$ is represented on an $S_L \times S_L$ grid, where S_L is the grid angular resolution, and that the 3D isotropic BRDF $\hat{\rho}(\theta_i, \theta_o, \phi)$ is represented on a grid of size $S_{\hat{\rho}} \times T_{\hat{\rho}} \times T_{\hat{\rho}}$ where $S_{\hat{\rho}}$ is the angular resolution with respect to θ_i and $T_{\hat{\rho}}$ is the angular resolution with respect to (θ_o, ϕ). For simplicity, we will consider the lighting and BRDF to be represented in latitude-longitude form, i.e. simply as tabulated values on an equally-spaced grid $0 \leq \theta \leq \pi$ and $0 \leq \phi \leq 2\pi$.

Our prefiltering algorithm computes the lighting coefficients L_{lm} to order F_L (i.e. F_L is the maximum value of l) and BRDF coefficients $\hat{\rho}_{lpq}$ to orders $F_{\hat{\rho}}$ and $P_{\hat{\rho}}$ (i.e. $l \leq F_{\hat{\rho}}$ and $p \leq P_{\hat{\rho}}$). The light field coefficients B_{lmpq} are computed to orders F_B and P_B. Finally, we generate the SHRM $B_{pq}(\alpha, \beta)$, with the angular size in (α, β) being $S_B \times S_B$, and the spherical harmonic expansion up to order P_B. Radially symmetric 1D BRDFs can be seen as special cases of this framework with $T_{\hat{\rho}} = 1$, and $P_{\hat{\rho}} = P_B = 0$.

5.1 Order of spherical harmonic expansions

We now analyze required orders F and P in our spherical harmonic expansions. First, consider the lighting. The total energy is

$$\int_{\theta=0}^{\pi} \int_{\phi=0}^{2\pi} L^2(\theta, \phi) \sin\theta \, d\theta d\phi = \sum_{l=0}^{\infty} \sum_{m=-l}^{l} \mid L_{lm} \mid^2$$

We can estimate the error ϵ in an order F_L spherical harmonic expansion by considering the fraction of the total lighting energy captured. To obtain an accuracy $1 - \epsilon$, we require that

$$\sum_{l=0}^{F_L} \sum_{m=-l}^{l} \mid L_{lm} \mid^2 \geq (1 - \epsilon) \int_{\theta=0}^{\pi} \int_{\phi=0}^{2\pi} L^2(\theta, \phi) \sin\theta \, d\theta d\phi$$

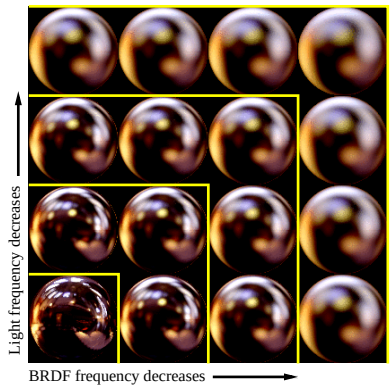

Figure 5: *Renderings with different lighting and BRDF conditions. The highest frequency in the images is approximately the minimum of the highest frequencies in the lighting and BRDF. Specifically, all spheres inside a yellow delimiter look similar.*

Given $L(\theta, \phi)$ and F_L, it is easy to determine the error ϵ, and check if it is below threshold. Conversely, if we fix ϵ, we can compute F_L as the minimum frequency for which the above equation holds. The number of coefficients required measures the frequency width of the signal, and ϵ measures the missing (residual) information. A similar method may be used for analyzing the BRDF.

The remaining issue is how to combine the information for lighting and BRDFs to determine appropriate orders for the reflected light field B. We list below two possible approaches.

- **Minimum of orders or errors:** Consider the case where $\epsilon = 0$ for either the lighting or BRDF, i.e. one or both is bandlimited. The reflected light field is then exactly reproduced by using an expansion to order $(F_B, P_B) = (\min(F_L, F_{\hat{\rho}}), P_{\hat{\rho}})$. This formalizes the intuition that we need to sample densely enough to catch the highest frequency present simultaneously in both the lighting signal and BRDF filter. This analysis does not apply rigorously when neither signal is bandlimited, but taking the minimum of orders for a given error ϵ is still a good heuristic. Conversely, for a given order of expansion, we can estimate the error $\epsilon_B = \min(\epsilon_L, \epsilon_{\hat{\rho}})$.

  Since the lighting signal usually contains substantial high frequency content, while the BRDF acts as a low-pass filter, this method often reduces simply to capturing $1 - \epsilon$ of the BRDF energy, i.e. choosing $F_B, P_B = F_{\hat{\rho}}, P_{\hat{\rho}}$ or setting $\epsilon_B = \epsilon_{\hat{\rho}}$.

- **Bound residual energy:** For completeness, we discuss a more rigorous numerical scheme, which can be proven to give conservative estimates. The scheme is based on bounding the residual unaccounted for energy in the reflected light field. One disadvantage of this method is that, unlike the previous method, we first need to actually calculate the coefficients B_{lmpq} of the reflected light field. Thus, this method is most useful as a final sanity check on the validity of the earlier heuristic. The mathematical details are in appendix B.

We use a simple example to illustrate these methods. For a particular illumination (the Grace Cathedral), and a Phong BRDF (exponent $s = 32$), we computed approximations to the lighting, BRDF, and reflected light field for increasing values of order $F = F_L = F_{\hat{\rho}} = F_B$. Since the BRDF is radially symmetric, $P = P_{\hat{\rho}} = P_B = 0$. We also computed the reflected light field accurately, by using a very high order $F = 30$, so we could determine the errors of lower-order approximations. Figure 6 plots the accuracy (top curve) of an order F approximation of B, as well as estimates of this accuracy obtained by taking the minimum of BRDF and light errors at order F, and by bounding the residual energy. We see that both accuracy estimates are conservative but fairly tight, especially for small errors or high accuracies (at higher frequencies). Further, taking the minimum of lighting and BRDF errors is almost always equivalent simply to using the BRDF error. Therefore, we choose the simplest approach of using the BRDF error, requiring $\epsilon_{\hat{\rho}}$ be lower than a user-selected tolerance.

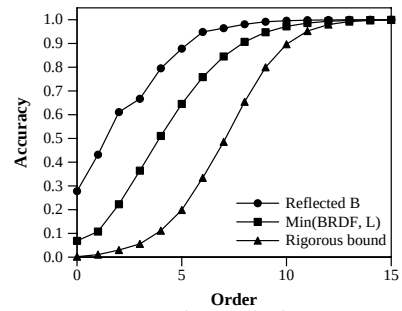

Figure 6: *Accuracy $(1-\epsilon)$ versus frequency F for an order F approximation of the reflected light field B, and estimates of that accuracy obtained by taking the minimum error for BRDF and lighting, and by using the conservative bound based on residual energy. We have not separately plotted using the BRDF error only, as this gives almost exactly the same curve as taking the minimum error for BRDF and lighting.*

5.2 Justification for SHRM representation

We seek to determine the best point in the spectrum of time/space or angular/frequency tradeoffs. For this, we must understand how to relate angular space resolutions S and T to frequency-space orders F and P. As a simple illustration, consider irradiance maps from Lambertian BRDFs. It has been shown [Basri and Jacobs 2001; Ramamoorthi and Hanrahan 2001b] that an order 2 spherical harmonic expansion suffices. However, a 3×3 irradiance map will clearly be inadequate. In practice, irradiance maps are usually represented at angular resolutions higher than 16×16. Experimenting with different resolutions, we have found that in general, one requires $S \sim 10F$ (and $T \sim 10P$).

Therefore, a significantly more compact size for B is obtained using spherical harmonic coefficients rather than an explicit 4D tabular representation. The other extreme in the spectrum of time-space tradeoffs—using a purely coefficient-based approach—is also usually[1] undesirable. Efficient rendering of 2D reflection maps having high frequency content, such as specular reflection maps from Phong BRDFs, is difficult directly from the spherical harmonic expansion, since $O(F^2)$ terms must be added per pixel, with F generally larger than 10. Rendering the 4D light field purely from coefficients is even harder, requiring $O(F^2P^2)$ terms.

Hence, we believe an intermediate representation, allowing for both compact representation, and fast rendering, is optimal. In order to determine the best representation for B, we must know the common values for orders F and P (and hence resolutions S and T). Our results in section 7 show that for practically all currently available analytic and measured BRDFs, values of $F \leq 30$ and $P \leq 5$ suffice for an accuracy greater than 90%. Therefore, it is best to encode the view dependence (θ_o, ϕ_o) as a compact (and easily evaluated) spherical harmonic expansion consisting of $(P+1)^2$ terms, while explicitly representing the high-frequency dependence on (α, β). This is the approach taken by SHRMs, where each pixel (α, β) stores coefficients $B_{pq}(\alpha, \beta)$ of an order P spherical harmonic expansion.

6 Prefiltering

We now describe our efficient frequency space prefiltering algorithms to create the SHRM and efficiently implement the pipeline in figure 3. We will present an analysis of the computational complexity of our algorithms, and end this section by validating our conclusions on the Phong BRDF.

6.1 Key steps and insights

Our prefiltering method has two main components. First, we must efficiently convert between angular and frequency space descriptions. Second, we must efficiently compute coefficients of the reflected light field from lighting and BRDF coefficients. Both components can be performed rapidly because of the insights below.

[1] For very diffuse BRDFs ($F_{\hat{\rho}}$ and $P_{\hat{\rho}}$ both very small), a purely coefficient-based approach may be acceptable. The most notable example is the Lambertian BRDF ($F_{\hat{\rho}} = 2$, $P_{\hat{\rho}} = 0$), where a 9 term spherical harmonic expansion suffices [Ramamoorthi and Hanrahan 2001a].

The algorithm itself is just a direct three step efficient implementation of the pipeline of figure 3. Implementation details, and the time complexities of the various steps, are found in appendix C.

Linear time complexity of convolution formula: The reflected light field coefficients B_{lmpq} can be computed in time *linear* in the number of output coefficients B_{lmpq} simply by applying the spherical convolution formula in equation 5.

Fast conversion to and from spherical harmonics: We still need to convert from an angular space representation of $L(\theta, \phi)$ and $\hat{\rho}(\theta_i, \theta_o, \phi)$ to the spherical harmonic coefficients, as well as generate the SHRM from B_{lmpq}. As an example, consider computation of lighting coefficients L_{lm}. For any l, m we have

$$L_{lm} = \int_{\theta=0}^{\pi} \int_{\phi=0}^{2\pi} L(\theta, \phi) Y_{lm}^*(\theta, \phi) \sin\theta \, d\theta d\phi$$

The cost of performing this integral is $O(S_L^2)$. Since we must do this for all coefficients, it would appear the total cost would be $O(F_L^2 S_L^2)$. In fact, we can amortize the cost to compute all the coefficients in $O(F_L S_L^2)$ time by writing the spherical harmonics as products of functions in θ and ϕ, and then separating the computations in θ and ϕ. The basic idea is to compute in succession:

$$\begin{aligned} \forall m, \theta: \quad L_m(\theta) &= \int_{\phi=0}^{2\pi} L(\theta, \phi) e^{-Im\phi} \, d\phi \\ \forall l, m: \quad L_{lm} &= \int_{\theta=0}^{\pi} L_m(\theta) f_{lm}(\theta) \sin\theta \, d\theta \end{aligned}$$

Here, the spherical harmonic $Y_{lm}(\theta, \phi) = f_{lm}(\theta) e^{Im\phi}$. The first step involves a loop over $(2F_L+1)S_L$ elements, each step of which requires numerical integration by adding together S_L values. Thus, the cost is $O(F_L S_L^2)$. A similar argument shows that the second step takes time of $O(F_L^2 S_L)$. Since $F_L < S_L$, the first step dominates, and the total complexity is $O(F_L S_L^2)$. Fast spherical harmonic transform methods [Mohlenkamp 1999], analogous to the Fast Fourier Transform, may reduce the cost further[2] to logarithmic in F_L, i.e $O(S_L^2 \log^2 S_L) \sim O(S_L^2 \log^2 F_L)$. However, these methods are complicated, and although asymptotically faster, have relatively large constant cost factors. Therefore, they are unlikely to be significantly faster for the relevant low frequencies $F \sim 30$.

6.2 Computational complexity

The cost of previous angular domain algorithms is $O(W S_L^2)$ per pixel in the output, since they perform a hemispherical integral for each pixel. Here, W is the fraction of the illumination pixels that need be considered, corresponding to the angular width of the BRDF, with $W \to 0$ for a mirror, and $W = 1/2$ if one considers the entire visible hemisphere. In appendix C, we derive the cost for our frequency space algorithm[3], which is much lower, being $O(F_B)$ or $O(P_B)$ per pixel. Table 3 summarizes our main results.

Type	Angular		Frequency	
	Cost	/pixel	Cost	/pixel
1D BRDF	$W S_L^2 S_B^2$	$W S_L^2$	$F_B S_B^2$	F_B
SHRM			$F_B P_B^2 S_B^2$	F_B
3D BRDF	$W S_L^2 T_B^2 S_B^2$	$W S_L^2$	$P_B T_B^2 S_B^2$	P_B

Table 3: *Computational complexity of prefiltering. We show both total costs and costs per pixel. The angular costs correspond to hemispherical integration, with W being the BRDF angular width. The frequency space costs are for our method.*

Radially Symmetric 1D BRDFs: The output reflection map size is $S_B \times S_B$. Standard hemispherical integration is *quadratic* in the output size, since we must examine $O(W S_L^2)$ illumination pixels per output pixel and[4] $S_L \geq S_B$. By contrast, our frequency space prefiltering algorithm requires only $O(F_B)$ time per output pixel. Since $F_B \ll S_B < S_L$, this method is only slightly *super-linear*, being substantially *sub-quadratic* in the output size.

[2]Since $S_L \sim 10F_L$, $\log S_L \sim \log F_L$. Also note that simply using an FFT in step 1 will not suffice, since step 2 does not have logarithmic complexity.

[3]If we were to use fast spherical harmonic transform methods, the asymptotic complexity per output pixel would be $O(\log^2 F_B)$ or $O(\log^2 P_B)$ instead.

[4]One way to compute F_B is $\min(F_L, F_{\hat{\rho}})$ so $F_B \leq F_L$ and $S_B \leq S_L$.

SHRM creation: The SHRM is a new representation, not created by traditional prefiltering algorithms. As for 1D BRDFs, the cost of our method is $O(F_B)$ per output pixel per coefficient.

3D BRDFs, explicit reflection maps: In order to compare to angular domain methods, we must produce the same output. We can use the SHRM to explicitly compute a set of $T_B \times T_B$ reflection maps (with $T_B \sim 10P_B$), similar to the explicit representations of Cabral et al. [Cabral et al. 1999] or Kautz and McCool [Kautz and McCool 2000][5]. The cost of traditional prefiltering remains $O(W S_L^2)$ per output pixel. On the other hand, our method takes $O(P_B)$ time per pixel. Since $P_B \leq 3$ in most cases, it can be regarded a constant. Hence, our method is *quasi-linear* in the output size. This is a speedup of three to four orders of magnitude—the difference between near-interactive computation in a few seconds, and prefiltering times in hours.

6.3 Validation with Phong BRDF

In this subsection, we validate our theoretical computational complexity analysis on the simple radially symmetric Phong model. In this case, $P_{\hat{\rho}} = P_B = 0$ and the SHRM reduces to a standard 2D reflection map $B(\alpha, \beta)$. In the results section, we show timings, including for more general 3D isotropic BRDFs.

The normalized and reparameterized Phong BRDF is defined by

$$\hat{\rho} = \frac{s+1}{2\pi} \cos^s \theta_i$$

where $\cos^s \theta_i = (\vec{R} \cdot \vec{L})^s$. BRDF coefficients $\hat{\rho}_l$ can be derived analytically [Ramamoorthi and Hanrahan 2001c], and an accurate approximation is

$$\hat{\rho}_l \approx \Lambda_l^{-1} \exp\left[-\frac{l^2}{2s}\right]$$

In appendix D, we show that the order $F_B = F_{\hat{\rho}}$ corresponding to error ϵ is $F_B = \sqrt{-s \log \epsilon}$. Ignoring the constant $\sqrt{-\log \epsilon}$, the prefiltering cost of our frequency space algorithm is therefore

$$C_f = O(F_B S_B^2) = O(S_B^2 \sqrt{s}) \tag{9}$$

Appendix D derives a formula for the angular width W of the BRDF, and shows that the angular domain prefiltering cost is

$$C_a = O(W S_L^2 S_B^2) = O\left(\frac{S_L^2 S_B^2}{s}\right) \tag{10}$$

We note that the frequency space cost C_f increases with increasing Phong exponent as $\sqrt{s}$, while the angular space cost C_a decreases with increasing Phong exponent as $1/s$. This is entirely expected, since sharp specular surfaces (large s) have a BRDF which is very local in the angular domain but requires a large number of coefficients to represent in the frequency domain. Conversely, rough surfaces (small s) are very easily handled in the frequency domain, but their BRDFs have a large angular width. Therefore, for $s < s^*$, our frequency domain methods are to be preferred and for $s > s^*$, conventional angular domain techniques are preferable. s^* can be found by equating equations 9 and 10.

$$S_B^2 \sqrt{s^*} \sim S_L^2 S_B^2 / s^* \Rightarrow s^* \sim S_L^{4/3}$$

What does this mean numerically? Assume a small size of $S_L = 100$. We then obtain $s^* \approx 464$. Therefore, in essentially all practical cases of interest, our frequency domain algorithm is superior to conventional angular domain methods, often by one to two orders of magnitude. Of course, the actual numerical value for s^* depends on the constant cost factors associated with the respective implementations. Our empirical tests, discussed in section 7.4, show that the practical value of s^* is actually even higher than predicted.

7 Results

We have tested our method using a number of different lighting conditions and BRDFs. This section reports our main results.

[5]Since their representation is 3D, we should compute only T_B reflection maps.

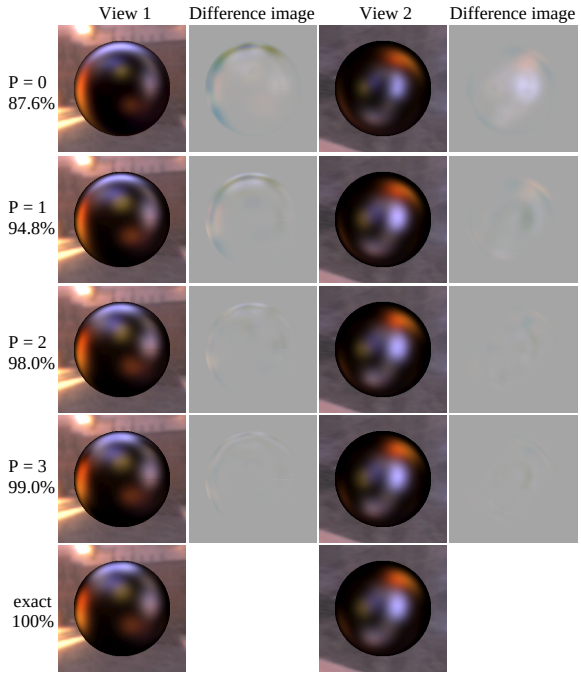

Figure 7: *Comparing images obtained with different values for P for a simplified microfacet BRDF model with surface roughness $\sigma = 0.2$. These images correspond to two particular views, i.e. values of $(\vec{\theta_o}, \vec{\phi_o})$. The percentages are fractions of the total energy $(1-\epsilon)$ of the BRDF captured for that P, which we use as a conservative estimate of the accuracy of the reflected light field. The exact images at the bottom were computed by a full hemispherical angular-space integral for each image pixel. For this and subsequent figures, the difference images are not amplified, and we used $F_B = 30$ and $S_B = 128$.*

7.1 Number of coefficients for analytic BRDFs

The practical values of the orders in the spherical harmonic expansion of the BRDF $F_{\hat{\rho}}$ and $P_{\hat{\rho}}$ (and hence F_B and P_B) will depend on the form of the BRDF, with slowly varying BRDFs requiring fewer coefficients. As a basic test to determine reasonable empirical values, we considered three general analytic BRDFs.

Microfacet: Consider a simplified microfacet [Torrance and Sparrow 1967] model,

$$\hat{\rho} = \frac{1}{4\pi\sigma^2} e^{-(\theta_h/\sigma)^2} \tag{11}$$

where $\theta_h = \cos^{-1}(\vec{N} \cdot \vec{H})$ is the angle between the normal and the half-angle vector. Approximations to reflection maps with different values of $P = P_{\hat{\rho}} = P_B$ are shown in figure 7. As expected, the accuracy improves as we use higher values of P. Specifically, $P = 2$ suffices to produce very accurate results, with the BRDF error $\epsilon < .03$. Recall from section 5.1 that we use the BRDF accuracy as a conservative estimate of the accuracy of the reflected light field. For this BRDF, $F = F_{\hat{\rho}} = F_B$ is given approximately by $F \sim \sigma^{-1}$, and ranges from 10 to 30 for common values of $\sigma \sim 0.1$. These values of F and P are typical for most BRDFs. In general, P is very small, while F is usually much larger.

Lafortune BRDF: We also tested the model of [Lafortune et al. 1997], with coefficients obtained from the skin measurements of Marschner et al. [2000]. Although the behavior is more interesting, with much stronger specularities exhibited toward grazing angles, a value of $P = 4$ still suffices for an error $\epsilon < .03$.

Kajiya-Kay model: Finally, we tried the Kajiya-Kay [1989] model, which is an anisotropic variant of the Phong BRDF, and depends on incident and outgoing angles with respect to the tangent vector. As discussed in section 3.1, we may reparameterize by the tangent vector, to derive $\hat{\rho} = \cos^s(\theta_i - \theta_o)$. While this paper does not consider general 4D anisotropic BRDFs, we can handle the Kajiya-Kay BRDF, since it is mathematically analogous to a (2D) isotropic BRDF after reparameterization. Unlike for ordinary Phong-like BRDFs, we cannot apply any further reflective reparameterization. Therefore, the value of P required is large (we found $P = 8$ for $s = 32$ and $\epsilon < .03$). However, there is no azimuthal dependence, so we require only $P+1$ terms $B_{p0}(\alpha, \beta)$ in the SHRM instead of $(P+1)^2$ (i.e. $q = 0$, with no dependence on ϕ_o). Hence, the SHRM is still a very efficient and compact representation.

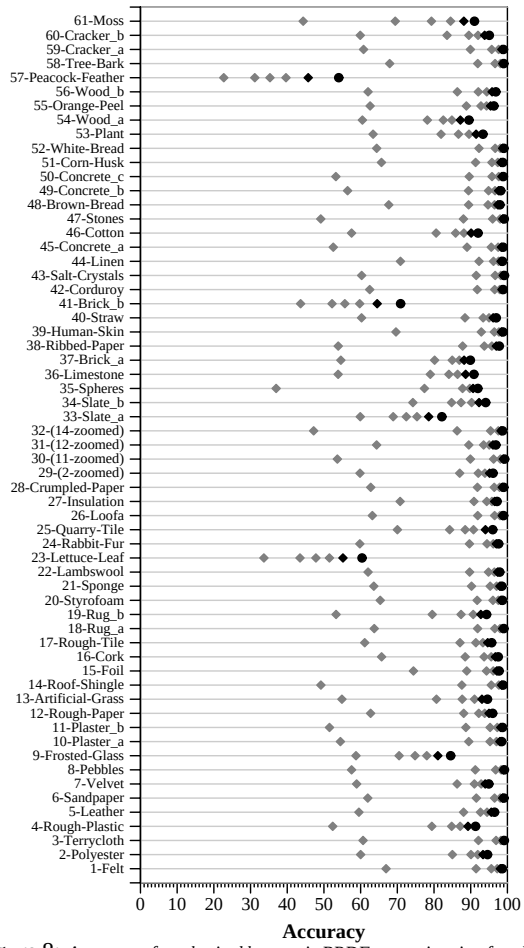

Figure 8: *Accuracy of a spherical harmonic BRDF approximation for all 61 BRDFs in the CURET database. We show 6 values of $P_{\hat{\rho}}$ ranging from 0 to 5 from left to right. The low orders for $P_{\hat{\rho}}$ are shown with light gray diamonds, while a black circle shows the highest order $P_{\hat{\rho}} = 5$. Note that the rightmost circle corresponds to an accuracy greater than 90% in 56 of the 61 rows.*

7.2 Number of coefficients for measured BRDFs

To further evaluate the accuracy of our approximations, we used the CURET database [Dana et al. 1999]. This database consists of 61 BRDFs and BTFs, corresponding to a variety of materials. For each sample, there are 205 BRDF measurements, which may be interpolated by fitting order 8 Zernike polynomials to create a complete BRDF description [Koenderink and van Doorn 1998].

Figure 8 is a bar chart showing, for each of the 61 samples, the accuracy of a BRDF approximation[6] with $F_{\hat{\rho}} = 30$ and values of $P_{\hat{\rho}}$ ranging from 0 to 5. In 56 cases, the accuracy for $F_{\hat{\rho}} = 30$ and $P_{\hat{\rho}} = 5$ was greater than 90% ($\epsilon < 0.1$), and was usually significantly higher (in most cases, $\epsilon < .05$ for $P_{\hat{\rho}} = 3$). The remaining 5 examples (9-frosted glass, 23-lettuce leaf, 33-slate a, 41-brick b, 57-peacock feather) were all significantly anisotropic.

Therefore, we conclude that for almost all BRDFs of interest, an order $P_B \leq 5$ suffices for the SHRM, with $F \leq 30$. In fact, for most BRDFs, a quadratic or cubic (second or third order with $P_B = 2$ or 3) spherical harmonic expansion in the SHRM suffices.

[6] We reparameterized all BRDFs by the reflection vector. Our results demonstrate that this reparameterization is suitable even if the BRDF is not primarily reflective, or consists of both diffuse and specular components. The specular components are compactly represented, while the diffuse components are low frequency anyway.

7.3 SHRM accuracy

We now compare images created with SHRMs to the correct image, and to previous approaches. First, figure 9 compares our method to Kautz and McCool's [2000] 3D texture-mapping technique[7], where they approximate the BRDF—and hence, the reflected light field—as having no azimuthal dependence. For the relatively complex velvet BRDF (CURET database) in figure 9, their approximation introduces large errors, while the SHRM with $P_B = 5$ is accurate.

Figure 10 compares our approach to the correct image and Cabral's icosahedral interpolation. For sharply-varying BRDFs, such as those exhibiting strong near-grazing specularities, or complex anisotropic behavior, Cabral's approximation can lead to large errors, while our approach still gives accurate results.

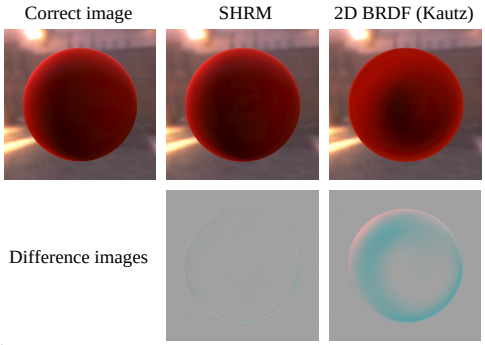

Figure 9: *Comparing the correct image on the left to those created using SHRMs (middle) and the 2D BRDF approximation of Kautz and McCool (right).*

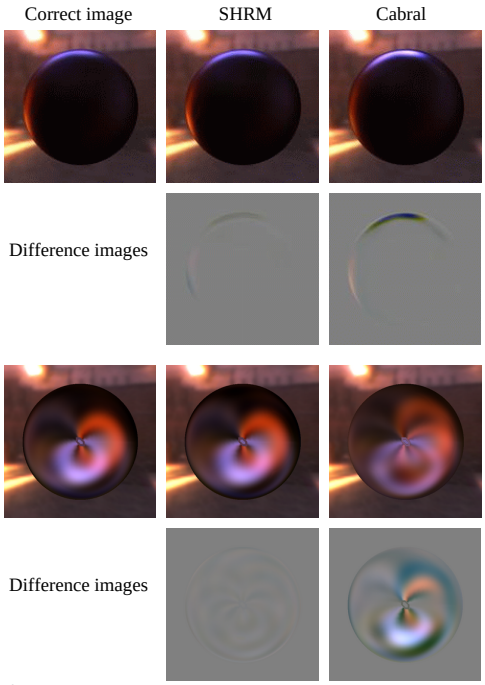

Figure 10: *Comparing the correct image to those created using SHRMs and icosahedral interpolation (Cabral's method). We see that the SHRM image is accurate, while Cabral's approximation is inadequate for sharp near-grazing reflections (top), and for complex BRDFs like the anisotropic Kajiya-Kay model (bottom).*

In our approach, the theoretical analysis can be used to systematically trade off accuracy for compactness and efficiency. Specifically, if Kautz and McCool's [2000] approximation of 2D BRDFs with no azimuthal dependence suffices ($q = 0$), we get a 3D SHRM with only $P_B + 1$ terms instead of $(P_B + 1)^2$. If Cabral et al.'s [1999] icosahedral set of 12 reflection maps suffices, we can use a very small number of terms ($P_B = 1$ or 2) in the SHRM.

[7] We use their single lobe model, with the BRDF being an arbitrary 2D function $\hat{\rho} = u(\theta_i, \theta_o)$. This is essentially equivalent to setting $q = 0$ in the local SHRM, using only the azimuthally independent terms.

7.4 Speed of prefiltering

We first consider Phong BRDFs, experimentally validating the theoretical conclusions of section 6.3. For our frequency domain algorithm, we used $\epsilon = .01$, conservatively setting $F_B = 1 + \sqrt{6s}$. For the angular domain, we were more aggressive, setting $\epsilon = .05$. The resolution S_L and S_B of the inputs and final results were 128, i.e. we generated output Phong reflection maps at 128×128 resolution. According to the theory, this is an appropriate resolution for $s = 32$ and $s = 64$ (i.e. $F_B \approx 12$), and is therefore the most suitable single resolution for the entire range of Phong exponents. The numerical running times reported in table 4 obviously depend on our implementation and hardware. However, we believe the *ratio* in running times of angular and frequency domain methods is quite representative. Furthermore, the timing data can be fit almost precisely to the theoretical predictions of equations 9 and 10. The results indicate that our prefiltering method is usually two orders of magnitude faster than angular-space methods, and that Phong BRDFs can be prefiltered at close to real-time rates using our approach.

Exponent s	Time (sec)		Ratio
	Angular	Frequency	(Ang/Freq)
8	67.28	0.081	830.6
16	38.03	0.114	333.6
32	21.80	0.159	137.1
64	11.94	0.227	52.6
128	7.17	0.328	21.9
256	3.55	0.461	7.7
512	2.28	0.686	3.3

Table 4: *Comparison of timings of angular and frequency-space prefiltering for different values of the Phong exponent s. The timings are on a 1.4GHz Pentium IV.*

As predicted by complexity analysis, the speedups are even more dramatic for the general case—illustrated using the microfacet model of equation 11. In table 5, we compare computation time for our approach and conventional methods. It can be seen that even the cost for creating the entire SHRM is much less than the cost of hemispherical integration for a single reflection map. When the cost to explicitly create multiple reflection maps is considered, our approach is three to four orders of magnitude faster.

σ	F_B, P_B	angular-space		frequency-space	
		Time (s)	Time/Image (s)	Time (s)	SHRM (s)
.1	24,3	923	9.23	2.70	1.55
.2	12,2	2744	27.44	1.55	0.72
.3	7,2	5731	57.31	1.49	0.67
.4	5,2	9034	90.34	1.47	0.65
.5	5,2	12580	125.80	1.45	0.64

Table 5: *Times for angular-space and our frequency-space prefiltering, with $T_B = 10$. The six columns are the value of the roughness σ, the order of expansion F_B, P_B for $\epsilon < .03$, the total angular-space computational time to create $T_B \times T_B = 100$ reflection maps, the angular-space time per reflection map, the total frequency-space time, and the frequency-space time for SHRM creation (but not explicit generation of reflection maps). Our approach is orders of magnitude faster, and even creation of the entire SHRM is usually faster than generating only a single image in angular space.*

7.5 Real-time rendering

There are several possibilities for real-time rendering. We could simply evaluate equation 6 in software for each pixel of the final image. If hardware multitexturing support is available, we may represent the spherical harmonics $Y_{pq}(\theta_o, \phi_o)$ and the local SHRM coefficients $B_{pq}(\alpha, \beta)$ by 2D texture maps. Since we are reparameterizing by the reflection vector, we will sometimes also refer to $B_{pq}(\alpha, \beta)$ as reflection maps. If $P_B = 2$, there would be 9 terms in the SHRM, corresponding to a total of 18 texture maps. We would then use graphics hardware to accumulate 9 terms, with each term being the product of two texture maps, i.e. $B_{pq}(\alpha, \beta) Y_{pq}(\theta_o, \phi_o)$. Since this algorithm is essentially that previously used for rendering factored BRDFs [Kautz and McCool 1999; McCool et al. 2001], the same code can now be easily adapted for arbitrary isotropic BRDFs and complex illumination.

A simpler approach is possible when the viewer can be assumed distant, using the global SHRM in equation 7. The spherical har-

monics $Y_{pq}(\tilde{\theta_o}, \tilde{\phi_o})$ need be evaluated only once per frame, for given viewpoint $(\tilde{\theta_o}, \tilde{\phi_o})$, instead of at each vertex or pixel. In fact, it is possible to render the scene using only a single reflection mapping pass. The key idea is to explicitly sum equation 7 to create a single dynamic 2D reflection map $\tilde{B}(\alpha, \beta)$, which is updated for every frame, i.e. each new viewpoint $(\tilde{\theta_o}, \tilde{\phi_o})$.

$$\tilde{B}(\alpha, \beta) = \sum_{p=0}^{P_B} \sum_{q=-p}^{p} \tilde{B}_{pq}(\alpha, \beta) Y_{pq}(\tilde{\theta_o}, \tilde{\phi_o}) \qquad (12)$$

Our implementation extends the Stanford real-time programmable shading system [Proudfoot et al. 2001] to render with global SHRMs using equation 12. An advantage of our approach is that standard reflection maps can be upgraded to SHRMs with no change in the external shader programs. Internally, we simply update the reflection map for each frame. We compute equation 12 in software, which allows us to easily consider high-dynamic range, and avoids hardware precision and clamping issues. In the figures, the high-dynamic range backgrounds are tone-mapped, but the objects themselves are computed and shaded using a linear scale.

We used a 1.4 GHz Pentium IV running Linux, with an NVIDIA Geforce2 GTS graphics card, for our tests. The reflection (cube)map $\tilde{B}(\alpha, \beta)$ was computed at a resolution of $64 \times 64 \times 6$, which is an appropriate resolution for most BRDFs, i.e. $F \sim 20$. Since there is real-time cube mapping hardware, the major cost is that for computing equation 12 in software per frame. We are able to achieve frame rates of approximately 30 frames per second, with real-time speeds even in scenes with multiple SHRMs. Figure 1 and the accompanying videotape show a number of examples.

8 Conclusions and Future Work

We have presented new frequency-space algorithms for real-time rendering of complex isotropic BRDFs under arbitrary distant illumination, and have validated our approach using many different BRDFs and lighting conditions. Our contributions include theoretical analysis that allows us to precisely determine the orders of our spherical harmonic expansions, the new compact and efficient SHRM representation for the reflected light field, and very fast prefiltering algorithms based on spherical harmonic transforms. We have integrated the three contributions into a complete frequency-space pipeline, as per figure 3. However, it is also easy to convert between SHRMs and previous explicit representations, as discussed in appendix C. Therefore, the contributions of this paper are relatively independent, and can also be incorporated separately.

There are several interesting similarities and differences between the SHRM and surface light field representations. In fact, the SHRM can be seen as a surface light field on a sphere. The main advantage is that the SHRM is independent of geometry. The disadvantage is that we do not capture effects due to spatially varying illumination, which includes non-uniform lighting, interreflection and self-shadowing. Since surface light fields are so large, they must be compressed. SHRMs expose the structure of the reflected light field in terms of the frequency properties of the illumination and BRDF. It is therefore interesting to compare spherical harmonic basis functions to PCA-based compression and factorization methods used for BRDFs [Kautz and McCool 1999] and surface light fields [Nishino et al. 1999; Wood et al. 2000]. The main advantage of SHRMs is that the theoretical analysis gives insight into the intrinsic complexity of the reflected light field. This allows us to directly compute the SHRM with the right order and resolution. On the other hand, PCA-based methods find an optimal basis to represent a data set, assuming no a priori knowledge, and are also usually more expensive. Standard PCA requires a dense 4D reflected light field as input, and an expensive singular-value decomposition. To efficiently create a more compact final representation, it it might be possible to run PCA directly on the SHRM.

One drawback of synthetic IBR is the long time required for precomputation, which precludes dynamic lighting or interactive manipulation of material properties. Our new prefiltering method takes an important step in addressing this problem for environment maps, and may be adapted in the future to rapidly compute synthetic surface light fields. For the special case of radially symmetric BRDFs, Kautz et al. [2000] have proposed using hardware-assisted 2D image convolution. However, while BRDFs are shift-invariant filters on the spherical domain, they are not shift-invariant in the plane, since projection on to a 2D image introduces distortion [Kautz et al. 2000], and may lead to inconsistencies—for instance, rotating the lighting may not correspond simply to rotating the prefiltered image. Our prefiltering algorithm can be viewed as spherical image processing on the incident illumination, convolving it with the BRDF filter. Our speedups are not surprising, given that planar image convolutions are often more efficiently computed in the Fourier domain. Other approaches to speed up prefiltering are hierarchical methods [Kautz et al. 2000] and spherical wavelets [Schröder and Sweldens 1995]. However, *there is no wavelet or hierarchical convolution formula*, so frequency domain methods are more appropriate for environment mapping.

In summary, natural illumination and accurate BRDFs are of growing importance in interactive applications, and this paper has presented a complete frequency-space pipeline to enable this.

Acknowledgements: Kekoa Proudfoot and Bill Mark helped us with details of the Stanford Real-Time Programmable Shading system, enabling us to implement SHRMs within its framework. Thanks also to Li-Yi Wei and Olaf Hall-Holt for reading early drafts. This work was supported in part by a Hodgson-Reed Stanford graduate fellowship and NSF ITR grant #0085864 "Interacting with the Visual World."

References

BASRI, R., AND JACOBS, D. 2001. Lambertian reflectance and linear subspaces. In *International Conference on Computer Vision*, 383–390.

BLINN, J., AND NEWELL, M. 1976. Texture and reflection in computer generated images. *Communications of the ACM 19*, 542–546.

CABRAL, B., MAX, N., AND SPRINGMEYER, R. 1987. Bidirectional reflection functions from surface bump maps. In *SIGGRAPH 87*, 273–281.

CABRAL, B., OLANO, M., AND NEMEC, P. 1999. Reflection space image based rendering. In *SIGGRAPH 99*, 165–170.

DANA, K., GINNEKEN, B., NAYAR, S., AND KOENDERINK, J. 1999. Reflectance and texture of real-world surfaces. *ACM Transactions on Graphics 18*, 1 (January), 1–34.

GREENE, N. 1986. Environment mapping and other applications of world projections. *IEEE Computer Graphics & Applications 6*, 11, 21–29.

HAKURA, Z., SNYDER, J., AND LENGYEL, J. 2001. Parameterized environment maps. In *ACM symposium on interactive 3D graphics*, 203–208.

KAJIYA, J., AND KAY, T. 1989. Rendering fur with three dimensional textures. In *SIGGRAPH 89*, 271–280.

KAUTZ, J., AND MCCOOL, M. 1999. Interactive rendering with arbitrary BRDFs using separable approximations. In *EGRW 99*, 247–260.

KAUTZ, J., AND MCCOOL, M. 2000. Approximation of glossy reflection with prefiltered environment maps. In *Graphics Interface*, 119–126.

KAUTZ, J., VÁZQUEZ, P., HEIDRICH, W., AND SEIDEL, H. 2000. A unified approach to prefiltered environment maps. In *EGRW 00*, 185–196.

KOENDERINK, J., AND VAN DOORN, A. 1998. Phenomenological description of bidirectional surface reflection. *JOSA A 15*, 11, 2903–2912.

LAFORTUNE, E., FOO, S., TORRANCE, K., AND GREENBERG, D. 1997. Non-linear approximation of reflectance functions. In *SIGGRAPH 97*, 117–126.

MACROBERT, T. 1948. *Spherical harmonics; an elementary treatise on harmonic functions, with applications*. Dover Publications.

MALZBENDER, T., GELB, D., AND WOLTERS, H. 2001. Polynomial texture maps. In *SIGGRAPH 01*, 519–528.

MARSCHNER, S., WESTIN, S., LAFORTUNE, E., TORRANCE, K., AND GREENBERG, D. 2000. Image-Based BRDF measurement including human skin. In *EGRW 00*, 139–152.

MCCOOL, M., ANG, J., AND AHMAD, A. 2001. Homomorphic factorization of BRDFs for high-performance rendering. In *SIGGRAPH 01*, 171–178.

MILLER, G., AND HOFFMAN, C. 1984. Illumination and reflection maps: Simulated objects in simulated and real environments. *SIGGRAPH 84 Advanced Computer Graphics Animation seminar notes*.

MOHLENKAMP, M. 1999. A fast transform for spherical harmonics. *The Journal of Fourier Analysis and Applications 5*, 2/3, 159–184.

NISHINO, K., SATO, Y., AND IKEUCHI, K. 1999. Eigen-texture method: Appearance compression based on 3D model. In *CVPR 99*, 618–624.

PROUDFOOT, K., MARK, W., TZVETKOV, S., AND HANRAHAN, P. 2001. A real-time procedural shading system for programmable graphics hardware. In *SIGGRAPH 01*, 159–170.

RAMAMOORTHI, R., AND HANRAHAN, P. 2001. An efficient representation for irradiance environment maps. In *SIGGRAPH 01*, 497–500.

RAMAMOORTHI, R., AND HANRAHAN, P. 2001. On the relationship between radiance and irradiance: Determining the illumination from images of a convex lambertian object. *JOSA A 18*, 10, 2448–2459.

RAMAMOORTHI, R., AND HANRAHAN, P. 2001. A signal-processing framework for inverse rendering. In *SIGGRAPH 01*, 117–128.
RUSINKIEWICZ, S. 1998. A new change of variables for efficient BRDF representation. In *EGRW 98*, 11–22.
SCHRÖDER, P., AND SWELDENS, W. 1995. Spherical wavelets: Texture processing. In *EGRW 95*, 252–263.
SILLION, F., ARVO, J., WESTIN, S., AND GREENBERG, D. 1991. A global illumination solution for general reflectance distributions. In *SIGGRAPH 91*, 187–196.
TORRANCE, K., AND SPARROW, E. 1967. Theory for off-specular reflection from roughened surfaces. *JOSA 57*, 9, 1105–1114.
WESTIN, S., ARVO, J., AND TORRANCE, K. 1992. Predicting reflectance functions from complex surfaces. In *SIGGRAPH 92*, 255–264.
WOOD, D., AZUMA, D., ALDINGER, K., CURLESS, B., DUCHAMP, T., SALESIN, D., AND STUETZLE, W. 2000. Surface light fields for 3D photography. In *SIGGRAPH 00*, 287–296.

Appendix A: Spherical signal processing

We summarize the important spherical signal processing results derived by Ramamoorthi and Hanrahan [2001b; 2001c]. This analysis uses spherical harmonics [MacRobert 1948], denoted here by $Y_{lm}(\theta,\phi) = f_{lm}(\theta)e^{Im\phi}$. We first consider the expansion of the BRDF. Here, $\phi = \phi_o - \phi_i$, and $\hat{\rho}_{lq,pq} = \hat{\rho}_{l-q,p-q} = \hat{\rho}_{lpq}$. U_q is a constant = 1 when $q = 0$ and 2 otherwise.

$$\begin{aligned}
\hat{\rho}(\theta_i,\phi_i,\theta_o,\phi_o) &= \sum_{l=0}^{\infty}\sum_{p=0}^{\infty}\sum_{q=-\min(l,p)}^{\min(l,p)} \hat{\rho}_{lq,pq} Y^*_{lq}(\theta_i,\phi_i) Y_{pq}(\theta,\phi_o) \\
\hat{\rho}(\theta_i,\theta_o,\phi) &= \sum_{l=0}^{\infty}\sum_{p=0}^{\infty}\sum_{q=0}^{\min(l,p)} U_q \hat{\rho}_{lpq} f_{lq}(\theta_i) f_{pq}(\theta_o)\cos q\phi \\
\hat{\rho}_{lpq} &= \int_{\theta_i=0}^{\pi}\int_{\theta_o=0}^{\pi}\int_{\phi=0}^{2\pi} K(\theta_i,\theta_o,\phi)\hat{\rho}(\theta_i,\theta_o,\phi)\, d\theta_i d\theta_o d\phi \\
K(\theta_i,\theta_o,\phi) &= 2\pi f_{lq}(\theta_i) f_{pq}(\theta_o)\sin\theta_i \sin\theta_o \cos q\phi \qquad (13)
\end{aligned}$$

The reflected light field $B(\alpha,\beta,\theta_o,\phi_o)$, defined by equation 2 in the angular domain, may now be computed as follows in the frequency domain:

$$B(\alpha,\beta,\theta_o,\phi_o) = \sum_{l=0}^{\infty}\sum_{m=-l}^{l}\sum_{p=0}^{\infty}\sum_{q=-p}^{p} B_{lmpq}\Lambda_l^{-1} D^l_{mq}(\alpha) e^{Im\beta} Y_{pq}(\theta_o,\phi_o)$$
$$B_{lmpq} = \Lambda_l L_{lm}\hat{\rho}_{lpq}$$

To avoid needing the constants Λ_l and Λ_l^{-1}, we will simply (re)define the coefficients $B_{lmpq} = L_{lm}\hat{\rho}_{lpq}$ in what follows. We may then expand the coefficients B_{lmpq} to compute the *local* SHRM $B_{pq}(\alpha,\beta)$.

$$\begin{aligned}
B_{pq}(\alpha,\beta) &= \sum_{l=0}^{\infty}\sum_{m=-l}^{l} B_{lmpq}\left(D^l_{mq}(\alpha)e^{Im\beta}\right) \\
B(\alpha,\beta,\theta_o,\phi_o) &= \sum_{p=0}^{\infty}\sum_{q=-p}^{p} B_{pq}(\alpha,\beta) Y_{pq}(\theta_o,\phi_o) \qquad (14)
\end{aligned}$$

Appendix B: Bound on residual energy

Consider an expansion to order F with errors for lighting and BRDF given by ϵ_L and $\epsilon_{\hat{\rho}}$. Denote the total BRDF and lighting energies by $\hat{\rho}_{tot}$ and L_{tot}. Since the reflected light field coefficients are simply a product of lighting and BRDF terms, the worst case for the residual energy occurs when it is all concentrated in mode $F+1$. This residual energy, denoted by B_{res}, and a conservative error estimate ϵ_B are

$$\begin{aligned}
B_{res} &= \Lambda_{F+1}\left(\epsilon_L L_{tot}\right)\left(\epsilon_{\hat{\rho}}\hat{\rho}_{tot}\right) \\
\epsilon_B &\le \frac{B_{res}}{\sum_{l=0}^{F}\sum_{m=-l}^{l}|B_{lm}|^2 + B_{res}}
\end{aligned}$$

This is for the radially symmetric case; in general, we simply use B_{lmpq} in place of B_{lm}. Note that ϵ_B tends to 0 as B_{res} tends to 0. But the latter quantity is a product of $\epsilon_{\hat{\rho}}$ and ϵ_L, and therefore always tends to 0 as F increases.

Appendix C: Prefiltering Algorithm

Step 1. Compute lighting and BRDF coefficients: We first compute the spherical harmonic coefficients of the BRDF using the following three step algorithm that efficiently implements equation 13.

$$\begin{aligned}
\hat{\rho}_q(\theta_i,\theta_o) &= 2\pi\int_0^{2\pi}\hat{\rho}(\theta_i,\theta_o,\phi)\cos q\phi\, d\phi \\
\hat{\rho}_{pq}(\theta_i) &= \int_0^{\pi}\hat{\rho}_q(\theta_i,\theta_o) f_{pq}(\theta_o)\sin\theta_o\, d\theta_o \\
\hat{\rho}_{lpq} &= \int_0^{\pi}\hat{\rho}_{pq}(\theta_i) f_{lq}(\theta_i)\sin\theta_i\, d\theta_i
\end{aligned}$$

The computational costs of the three terms in the above sequence are, respectively, $O(P_{\hat{\rho}}S_{\hat{\rho}}T^2_{\hat{\rho}})$, $O(P^2_{\hat{\rho}}S_{\hat{\rho}}T_{\hat{\rho}})$, and $O(F_{\hat{\rho}}P^2_{\hat{\rho}}S_{\hat{\rho}})$. Since $P_{\hat{\rho}} < T_{\hat{\rho}}$, the first term dominates the second, and the net cost is $O\left(P_{\hat{\rho}}S_{\hat{\rho}}(T^2_{\hat{\rho}} + F_{\hat{\rho}}P_{\hat{\rho}})\right)$. For most non radially-symmetric BRDFs, $T^2_{\hat{\rho}} > F_{\hat{\rho}}P_{\hat{\rho}}$ (for instance, use $T_{\hat{\rho}} \sim 10$, $F_{\hat{\rho}} \sim 20$ and $P_{\hat{\rho}} \sim 3$), so the first term dominates and the total cost is $O(P_{\hat{\rho}}S_{\hat{\rho}}T^2_{\hat{\rho}})$.

If our error tolerance ϵ is satisfied, we see how far $P_{\hat{\rho}}$ can be reduced to still satisfy the error tolerance, and then also reduce $F_{\hat{\rho}}$ as much as possible. We can then set F_B and P_B according to the minimal values of $F_{\hat{\rho}}$ and $P_{\hat{\rho}}$. If the error is initially larger than ϵ, we repeat the algorithm with larger values for $F_{\hat{\rho}}$ and $P_{\hat{\rho}}$. Since computing BRDF coefficients is not the dominant algorithm cost, this recomputation does not significantly affect the total time, nor does using large initial values for $F_{\hat{\rho}}$ and $P_{\hat{\rho}}$.

Finally, we compute the lighting coefficients in time $O(F_B S^2_L)$. Note that we have already determined F_B, so we are not required to consider higher frequencies for the lighting, which is why we use F_B instead of F_L.

Step 2. Find reflected light field coefficients: We now find B_{lmpq} by directly using equation 5 in time $O(F^2_B P^2_B)$.

Step 3. Compute SHRM: We now compute the local SHRM by efficiently implementing equation 14. From this, we can compute the *global* SHRM $B_{pq}(\alpha,\beta)$ using equation 8.

$$\begin{aligned}
B_{mpq}(\alpha) &= \sum_{l=|m|}^{F_B} B_{lmpq} D^l_{mq}(\alpha) \\
B_{pq}(\alpha,\beta) &= \sum_{m=-F_B}^{F_B} B_{mpq}(\alpha) e^{Im\beta}
\end{aligned}$$

The costs of the two terms in the above sequence are $O(F^2_B P^2_B S_B)$ and $O(F_B P^2_B S^2_B)$. Since $S_B > F_B$, the net cost is $O(F_B P^2_B S^2_B)$. The cost for this step is also the dominant cost for the entire algorithm.

Radially symmetric BRDFs: For the special case of BRDFs like Lambertian and Phong models, $T_{\hat{\rho}} = 1$ and $P_{\hat{\rho}} = P_B = 0$. Technically, the complexity formulae above should use $P+1$ instead of P, to yield meaningful results for radially symmetric BRDFs. For these models, step 1 takes time of $O(F_{\hat{\rho}}S_{\hat{\rho}})$ to compute BRDF coefficients $\hat{\rho}_l$, and time $O(F_B S^2_L)$ to compute lighting coefficients L_{lm}. Step 2 takes $O(F^2_B)$ time. Finally, the SHRM in step 3 includes only the constant term and is therefore a simple reflection map $B(\alpha,\beta)$, computed in time $O(F_B S^2_B)$. The dominant cost here is to convert to and from spherical harmonic representations. Assuming we downsample the environment map if necessary so $S_L \sim S_B$, the total time is $O(F_B S^2_B)$ or $O(F_B)$ per output image pixel.

Conversion between SHRMs and explicit forms: It is possible to incorporate the prefiltering and rendering phases of our algorithm separately into existing systems. SHRMs may be created from explicit representations simply by fitting coefficients or integrating. If the implementer wants to use only our fast prefiltering method, but render using previous explicit representations, they can compute tabular representations from SHRMs. Cabral's twelve prerendered reflection maps may be computed very rapidly using equation 12, with $(\tilde{\theta_o}, \tilde{\phi_o})$ set to vertices of an icosahedron. Kautz and McCool's [2000] 3D texture is computed by expanding

$$B(\alpha,\beta,\theta_o) = \sum_{p=0}^{P_B} B_{p0}(\alpha,\beta) Y_{p0}(\theta_o)$$

This takes time $O(P_B)$ per output texel. Using fast conversion methods, we can also explicitly generate $T_B \times T_B$ reflection maps (a full 4D light field) in time $O(P_B)$ per output pixel, for a total cost of $O(P_B T^2_B S^2_B)$.

Appendix D: Costs for Phong BRDF

In the frequency domain, the order $F = F_B = F_{\hat{\rho}}$ for an error ϵ is found by

$$\begin{aligned}
\sum_{l=0}^{F}\hat{\rho}_l^2 &= (1-\epsilon)\sum_{l=0}^{\infty}\hat{\rho}_l^2 \\
\int_0^F l e^{-l^2/s}\, dl &\approx (1-\epsilon)\int_0^{\infty} l e^{-l^2/s}\, dl \\
1 - e^{-F^2/s} &\approx 1-\epsilon \\
F &\approx \sqrt{-s\log\epsilon}
\end{aligned}$$

In the angular domain, we may truncate the BRDF, so $(1-\epsilon)$ of the angular domain energy lies in $\theta_i \le \theta_i^*$. We find the angular width W and θ_i^* by

$$\begin{aligned}
\int_0^{\theta_i^*}\cos^s\theta_i \sin\theta_i\, d\theta_i &= (1-\epsilon)\int_0^{\pi/2}\cos^s\theta_i\sin\theta_i\, d\theta_i \\
1-\cos^{s+1}\theta_i^* &= 1-\epsilon \\
\cos\theta_i^* &= \epsilon^{1/(s+1)} \\
W = \frac{2\pi}{4\pi}\int_0^{\theta_i^*}\sin\theta_i\, d\theta_i &= \frac{1}{2}\left(1-\epsilon^{1/(s+1)}\right)
\end{aligned}$$

We now assume s is large ($1/s \to 0$) and perform a Taylor series expansion:

$$W \sim \left(1-\epsilon^{1/(s+1)}\right) = \left(1-\left[1+\frac{\log\epsilon}{s+1}\right]\right) \approx \frac{-\log\epsilon}{s}$$